Research Article | Vol. 28, No. 14 / 6 July 2020 / Optics Express 19887
Optics EXPRESS

Thermally stable monolithic Doppler asymmetric spatial heterodyne interferometer: optical design and laboratory performance

DAIKANG WEI,[1,2] YAJUN ZHU,[3,5] JILIN LIU,[4] QIUCHENG GONG,[1,2] MARTIN KAUFMANN,[1,2,6] FRIEDHELM OLSCHEWSKI,[2] PETER KNIELING,[2] JIYAO XU,[3] RALF KOPPMANN,[2] AND MARTIN RIESE[1,2]

[1]*Institute of Energy and Climate Research (IEK-7), Jülich Research Centre, Jülich 52425, Germany*
[2]*Institute for Atmospheric and Environmental Research, University of Wuppertal, Wuppertal 42119, Germany*
[3]*National Space Science Center, Chinese Academy of Sciences, Beijing 100190, China*
[4]*Qian Xuesen Laboratory of Space Technology, China Academy of Space Technology, Beijing 100094, China*
[5]*y.zhu@swl.ac.cn*
[6]*m.kaufmann@fz-juelich.de*

Abstract: We report on a thermally stable monolithic Doppler asymmetric spatial heterodyne (DASH) interferometer with field-widening prisms for thermospheric wind measurements by observing the Doppler shift of the airglow emission. Analytical deduction and numerical simulation are applied to determine the central optical path difference, the thermal compensation condition and the field-widening design. A monolithic interferometer with optimized configuration was built and tested in the laboratory. Laboratory tests show that the best visibility of 0.94 was realized with the 9 ° field-of-view illumination, while the thermal responses of the spatial frequency and the optical phase offset are 0.0154 $cm^{-1}/^{\circ}C$ and 0.469 rad/°C, respectively.

1. Introduction

Atmospheric winds play an important role in atmospheric dynamics and energetics. Thermospheric neutral winds impact on the interaction between neutral molecules and plasmas, which is relevant for space weather forecasts and modern satellite communications [1–4]. A passive wind detection technique is generally implemented in measuring the middle and upper atmospheric winds by observing the Doppler shift of natural emission lines. In this region, the airglow lines emitted by atomic oxygen and molecular oxygen can be found, and the Doppler shift of lines can be used as targets to measure the thermospheric winds.

Doppler-shift measurements of thermospheric winds using the passive optical technique have been carried out in the past few decades [5–8]. Fabry-Perot interferometers (FPI) have been widely used to measure the thermospheric winds due to their high sensitivity and simple configuration [5,6,9]. However, extreme manufacturing tolerance (smaller than $\lambda/20$) of the etalon results in high costs, and its inevitably large and heavy volume to achieve good optical throughput further constrains its application. Another typical instrument, the Michelson interferometer (MI), monitors the phase shift in the interferograms to trace the Doppler shift. The characteristics of field widening and thermal compensation greatly improve measurement responsivity and accuracy, even if only a few phase points of the interferogram are sampled during one scanning period [7,8]. On the other hand, an ultra-narrow prefilter needs to be employed in isolating the

#394101 https://doi.org/10.1364/OE.394101
Journal © 2020 Received 2 Apr 2020; revised 9 Jun 2020; accepted 9 Jun 2020; published 22 Jun 2020

Optics EXPRESS

single airglow emission line. Stringent scanning stability and accuracy are also required for an MI instrument.

Spatial heterodyne spectroscopy (SHS) is an effective methodology to achieve a high-resolution spectrum using stationary interference fringes and is similar to the MI system with two diffraction gratings replacing the reflection mirrors. Its features of high throughput owing to the field-widening design and no moving parts mean that the SHS instrument is particularly suited to the spectroscopy of weak diffuse emissions such as atmospheric airglow [10,11]. Lengthening the optical path on one arm transforms an SHS interferometer into a Doppler asymmetric spatial heterodyne (DASH) interferometer. This simple modification makes it possible to sample hundreds of phase points around a large optical path difference (OPD) without moving components [12]. Owing to the fact that a DASH interferometer can resolve multiple emission lines simultaneously, it is possible to use a reference line to track thermal changes to the instrument. A DASH technique combining the advantages of MI and SHS was recently developed to probe thermospheric winds. Harlander et al. designed a monolithic DASH interferometer based on a Köster's double-reflection prism [13], and ground-based observations of atomic oxygen red line emission (λ = 630 nm) were successfully conducted [14]. The Michelson Interferometer for Global High-Resolution Imaging of the Thermosphere and Ionosphere (MIGHTI), an instrument on NASA's Ionospheric Connection Explorer (ICON) satellite using the DASH technique, was developed to measure thermospheric winds and temperature [15,16].

In order to study the evolution of mesospheric or thermospheric phenomena, global network observations of thermospheric winds are routinely carried out [9,17,18]. A more inexpensive and precise instrument is expected to replace the typical FPI instrument. A thermally compensated DASH instrument is one of the potential candidates. To resolve the winds within an accuracy of 3m/s, wavelength shifts smaller than 9 orders of magnitude of the emission wavelength have to be detected. Therefore, the phases of the fringes must be highly stable with respect to ambient temperature, especially for the ground-based instrument which needs relatively long exposure times (usually 3-5 minutes) to collect enough photons.

In this paper, a thermally insensitive monolithic DASH interferometer with field-widening prisms for measuring thermospheric winds, by observing the Doppler shift of the atomic oxygen airglow at the wavelength of 630.0 nm, is discussed including the optical design and laboratory performance. Firstly, the detection concept of a ground-based DASH instrument is presented in Section 2. In Section 3, the optical design is systematically described from the aspects of choice of optimum OPD offset, thermal compensation, field widening, and configuration optimization. Section 4 discusses the characteristics of the interferometer as built in the laboratory including the fringe visibility and Littrow angle. To evaluate the thermal performance, the sensitivities of the spatial frequency and the optical phase are characterized based on measurement and model study in Section 5. Finally, a discussion and conclusions are presented in Section 6.

2. Detection concept

A conventional field-widening DASH interferometer is shown in Fig. 1. Incoming radiation is divided into two coherent wavefronts by the beamsplitter. After reflection from the gratings, these two wavefronts with an intersection angle of 2γ recombine on the detector producing a Fizeau fringe pattern, where the zero OPD point shifts from the center to some place on one side due to the additional length Δd on one arm. The recorded interferogram at position x can be expressed as

$$I(x) \propto 1 + V_I(x) \cos\left\{2\pi\left[4\tan\theta\left(\sigma_0 - \sigma_L\right)x + 2\sigma_0\Delta d_0\right]\right\} \exp\left[-2\pi^2\sigma_D^2\left(D + 4\tan\theta x\right)^2\right], \quad (1)$$

where $V_I(x)$ is the instrument visibility function, σ_0 is the wavenumber of the emission line, θ is the Littrow angle with respect to the grating Littrow wavenumber σ_L, σ_D is the Doppler-broadening parameter, and Δd_0 is the extended distance at the central wavelength of the emission

Optics EXPRESS

line [19]. D represents the effective OPD, which is defined to replace the fixed OPD offset ($2\Delta d$) when the optical dispersion is considered [19]. The phase difference between the interferograms obtained from zero-wind measurement and Doppler-wind measurement has the relation below

$$\Delta\varphi(x) = 8\pi \tan\theta x\sigma_0 \frac{v}{c} + 2\pi D\sigma_0 \frac{v}{c}, \tag{2}$$

where c represents the speed of light [19]. Accordingly, the Doppler velocity v can be retrieved.

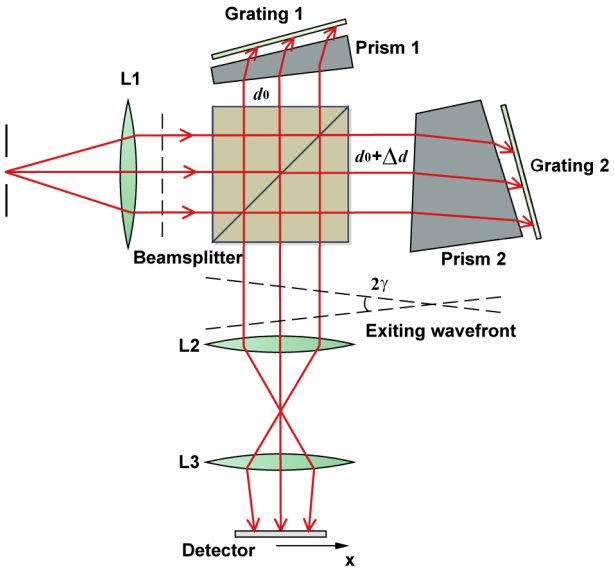

Fig. 1. Schematic of a field-widening DASH interferometer. L1 denotes the fore optics, L2 and L3 denote the exiting optics, and the arrow denotes the x direction on the detector. d_0 and $d_0 + \Delta d$ represent the optical paths from the beamsplitter to the gratings on the arm one and arm two, respectively.

Figure 2 presents the field-measurement strategy of a ground-based DASH instrument. In order to detect the horizontal wind velocity, sequential measurements viewing zenith, eastward

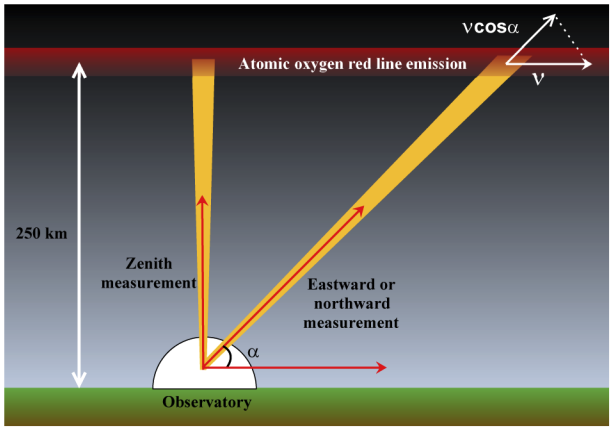

Fig. 2. Measurement strategy of a ground-based DASH instrument. Note that α represents the elevation angle and v represents the horizontal wind velocity.

Optics EXPRESS

and northward are performed. The zenith measurements are used for zero-wind calibration, which assumes that the average vertical wind throughout the night is zero [20]. After determining the Doppler velocity, the horizontal wind are finally calculated by dividing the line-of-sight velocity by the cosine of the elevation angle.

3. Optical design

3.1. Choice of OPD offset

According to the phase-difference relation as shown in Eq. (2), a DASH interferometer becomes more sensitive when its OPD goes to a larger number. On the other hand, the visibility of the fringe pattern, a leading factor to detect periodic waves in the presence of noise, decreases with the increment of OPD due to the contribution of the exponential term in Eq. (1). The contradiction between small and large OPD values indicates that an optimum OPD offset can be found for the best measurement of winds.

Numerical studies have been carried out to determine the OPD offset. Given an OPD offset, the interferogram of the atomic oxygen red line can be produced using Eq. (1) with a typical temperature (1000 K) broadening. The noise can be added to the interferogram based on the estimated signal-to-noise ratio, which is calculated from the volume emission rate, system etendue, optics transmission and detector characterization. The volume emission rate was calculated based on a model developed by Cogger et al. [21,22]. With the 500-row pixel average and 5-minute exposure time, 10000 Monte Carlo simulations (adding noise) were performed for each OPD. Then the estimation error of the wind speed as a function of different OPD was deduced, which is the average result of all simulations. The phase comparison between two interferograms was accomplished by the Hilbert transform described in [19]. The numerical result in Fig. 3 indicates that the minimum wind estimation error can be achieved when the OPD offsets are in the range of 30 mm to 50 mm.

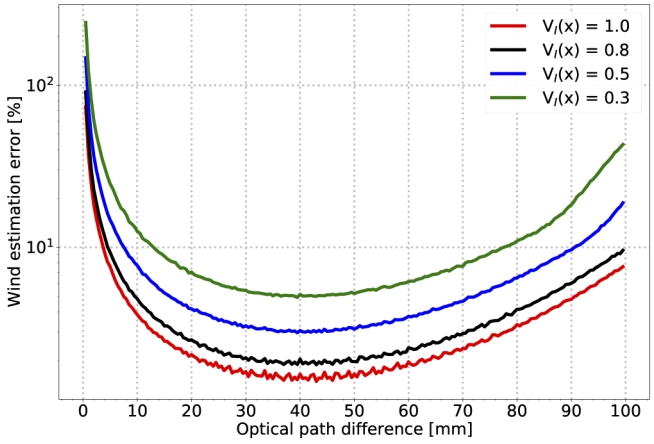

Fig. 3. Error of wind estimation as a function of the OPD value. The pixel number is 2048×2048, and the wind velocity is 100 m/s in the simulaiton.

3.2. Thermal compensation

The Doppler wind is measured by comparing the phase differences, which are highly sensitive to ambient temperature around the instrument. For the 32 mm OPD offset, a thermal drift of less than 3.2 mrad is required to achieve 3 m/s accuracy. The thermal drift not only introduces the additional phase error but also deteriorates the fringe contrast especially when a relatively

Optics EXPRESS

longer exposure time is required. Choosing the correct combination of glasses and dimensions can achieve thermally stable performance, which has already been employed in MI instruments [23,24]. The phase independence of the surrounding heat requires the derivation of the phase with respect to temperature to be zero, and the expression can be written according to Eq. (1)

$$\frac{d\varphi(x)}{dT} = 2\pi\left(\frac{df_x}{dT}x + 2\frac{d\Delta d_0}{dT}\sigma\right) = 0, \tag{3}$$

with the temperature T and the spatial frequency $f_x = 4\tan\theta(\sigma - \sigma_L)$. This equation holds when the two derivative terms $\frac{df_x}{dT}$ and $\frac{d\Delta d_0}{dT}$ are equivalent to zero at the same time.

For the $\frac{df_x}{dT}$ term, substituting grating transmission equation yields the temperature-independent spatial frequency condition

$$\alpha_{CTE} = -\frac{dn}{dT}\frac{n\sin\alpha}{\tan\theta\cos\phi\sqrt{n^2 - \sin^2\beta}}, \tag{4}$$

where n and α_{CTE} represent the refractive index of prism and the thermal expansion coefficient of the grating substrate, respectively. As shown in Fig. 4(a), β is the incident angle in the first plane of prism, α is the apex angle of prism, and ϕ is the exit angle in the second plane of prism. Thus, a suitable material with a negative derivative of the refractive index with respect to the temperature employed in the field-widening prism can mitigate the influence from the grating thermal expansion.

$\frac{d\Delta d_0}{dT} = 0$ makes the additional OPD of the interferometer independent of ambient temperature at a given wavelength. As shown in Fig. 4(b), the difference of the beamsplitter and spacers on two arms provides the OPD. For a monolithic DASH, the beamsplitter, prisms and the gratings are contacted with the spacers made of optical glasses, so that the thermal expansion of the spacers also affects the OPD. Consequently, the temperature-independent OPD offset condition can be expressed as

$$\frac{d\Delta d_0}{dT} = \frac{dn_1}{dT}t_1 + n_1\alpha_1 t_1 + \alpha_2 d_1 - \alpha_3 d_2 = 0, \tag{5}$$

where n_1 is the beamsplitter refractive index, t_1 is the asymmetric thickness of beamsplitter, $d_{1,2}$ are the thicknesses of spacer 1 and spacer 2, respectively, and $\alpha_{1,2,3}$ are the thermal expansion coefficients of the beamsplitter, spacer 1, and spacer 2, respectively.

3.3. Field widening

The field-widening technique greatly increases the ability to receive radiation from a relatively large solid angle with high fringe contrast. This has already been applied in SHS and DASH interferometers [12,25]. Inserting prisms with a certain apex angle can compensate the OPD differences arising from the different incident angles. In a DASH system with a field-of-view solid angle Ω, the fringe intensity as a function of position x can be expressed as

$$I(x) = \int_{-\infty}^{+\infty}\int_{0}^{\Omega_m} B(\sigma)\left\{1 + \cos 2\pi\left[4\tan\theta\left(\sigma - \sigma_L - \frac{\Omega\sigma}{2\pi}\right)x + 2\Delta d_0(\omega)\sigma\right]\right\} d\Omega d\sigma, \tag{6}$$

where $B(\sigma)$ is the input spectral intensity and ω is the incident angle in the spacer [26]. The presence of the OPD differences changing with the off-axis angle limits the field of view and degrades the contrast of the interferogram, which explains the $VI(x)$ term in Eq. (1). In this case,

Optics EXPRESS

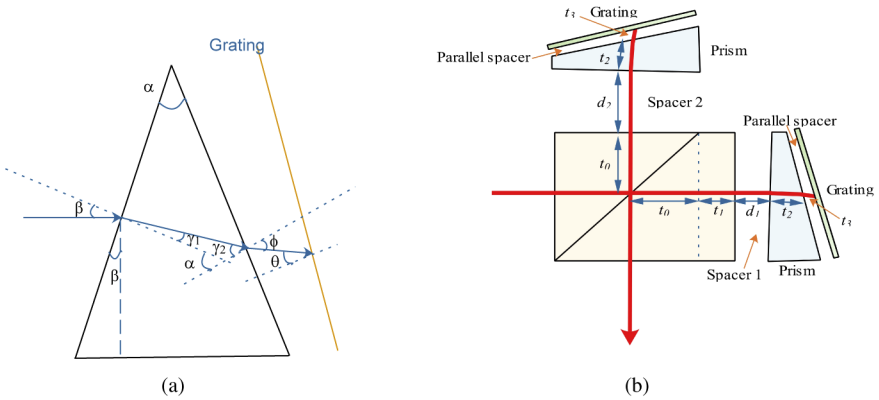

Fig. 4. Ray trace on a field-widening prism and a reflecting grating for the case of on-axis (a) and a thermally compensated field-widening DASH interferometer with an asymmetric beamsplitter (b).

the OPD offset Δd_0 as a function of incident angle ω can be written as

$$\Delta d_0(\omega) = n_1 t_1 + d_1 - d_2 - \frac{\sin^2 \omega}{2}\left(\frac{t_1}{n_1} + d_1 - d_2\right) - 0\left(\sin^4 \omega\right) + \cdots . \tag{7}$$

In order to achieve field-widening applications eliminating the effect from angle ω, the second order term should be set to zero, yielding

$$\frac{t_1}{n_1} + d_1 - d_2 = 0. \tag{8}$$

From a geometric optics point of view, the images of the gratings on the two arms are coincident viewed from the exit pupil as Eq. (8) requires.

In addition, the spatial frequency of the fringe varies with the field of view due to the term $\frac{\Omega\sigma}{2\pi}$ in Eq. (6). Harlander et al. inserted prisms in an SHS configuration to achieve field widening [26], which also works here to eliminate the term $\frac{\Omega\sigma}{2\pi}$. Because of the transmission difference on the dispersion plane and the reflection plane of the grating, it is difficult to find a general expression to determine the prisms, whereas an optimization approach can be an alternative. Assuming an optical phase change $\Delta\varphi(x)$, which is the phase difference between the on-axis and off-axis rays, optimizing the prisms' angles and dimensions to minimize $\Delta\varphi(x)$ can achieve the best field-widening performance.

3.4. Configuration optimization

Thermal compensation theory and field-widening analysis make it possible to optimize the DASH interferometer parameters. We segment the field of view into several small angles, and then the corresponding phase differences $\Delta\varphi(x)$ at different angles are traced by ray-trace software. With a damped least squares algorithm, minimizing the phase differences under the constraints of Eq. (4), Eq. (5) and Eq. (8) yields an interferometer design shown in Table 1. The collocation of the asymmetric beamsplitter, the spacers and the identical field-widening prisms provides the 32 mm OPD offset and also maintains the coincidence of two grating images. Due to the negative value of $\frac{dn}{dT}$ at the working wavelength, N-LAK12 glass was chosen for the field-widening prisms to stabilize the spatial frequency. Spacer 1 has a smaller thermal expansion coefficient

Optics EXPRESS

and a thinner dimension, while spacer 2 has a higher thermal expansion coefficient and a thicker dimension. These different expansions on the two arms compensate the OPD variation with the parameter $\frac{d\Delta d_0}{dT}$ of 1.2×10^{-7} mm/°C, which corresponds to 1.2 mrad uncertainty per °C. In recent monolithic DASH systems, the spacers were fabricated as hollow frames to connect the beamsplitter, the field-widening prisms and the gratings on the one hand and not to block beam transmission on the other hand [13,15]. Here two separate prisms are applied to replace the frame, which reduces the mechanical deformation caused by the differential thermal expansion between different materials. In addition, a series of through holes are drilled on the prisms of spacers to further relieve the strain. Note that all of the parameters in Table 1 refer to an environment of 25 °C and 1013 hPa.

Table 1. Specification of Design Parameters

Full field of view	9°
Etendue	0.156 cm^2steradian
Beamsplitter	Asymmetric beamsplitter
Material	Schott N-BK7
Beamsplitting coating	50/50 nonpolarizing
Field-widening prisms	Two prisms are identical
Material	Schott N-LAK12
Apex angle	15.114°
Wedged spacers	Holey spacers
Material	Fused silica (Spacer 1), CD H-FK61 (Spacer 2)
Parallel spacers	Holey spacers
Material	Fused silica
Gratings	Plane ruled reflectance gratings
Blank material	Fused silica
Groove density	900 mm^{-1}
Littrow angle	16.4950°
Optical path difference at center $2\Delta d_0$	32 mm
$\frac{d\Delta d_0}{dT}$ [mm/°C]	1.2×10^{-7}

4. Property characterizations

As shown in Fig. 5, a monolithic DASH interferometer was built in the laboratory. To characterize this interferometer, a breadboard system was constructed illustrated in Fig. 6. After passing through the rotating disk, the narrow linewidth laser was focused into the sphere by lens L4, which then generates a uniform distribution on the output port of the integrating sphere by multiple scattering reflections. A baffle was inserted between the integrating sphere and the interferometer to eliminate the stray light, so that the uniform radiation within the desired field of view illuminates the interferometer. Owing to the low distortion and stable performance, telecentric lenses with a magnification of 1.0 are applied to image the fringes from the localization plane onto the array detector. Note that the role of the rotating disk is to suppress laser speckle because the emergence of speckles can deteriorate the fringe pattern.

As shown in Fig. 7(a), a fringe image was recorded when the interferometer viewed the output port of the integrating sphere. The image distortion in the fringe pattern is almost negligible due to the excellent performance of the double telecentric lenses. The big issue is the stripe tilt in the Y direction caused by the misalignment during assembly. The existence of the Y-direction

Optics EXPRESS

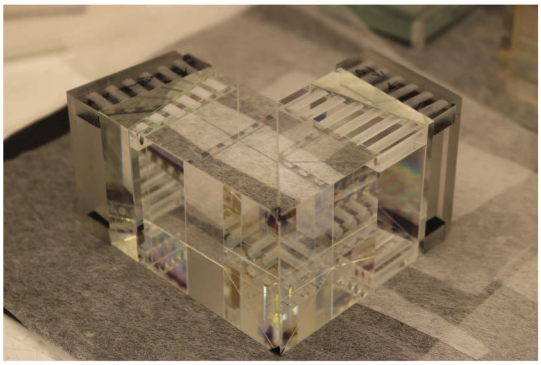

Fig. 5. The monolithic DASH interferometer. Each spacer, including spacer 1, spacer 2 and parallel spacers, consists of two identical prisms with several through holes.

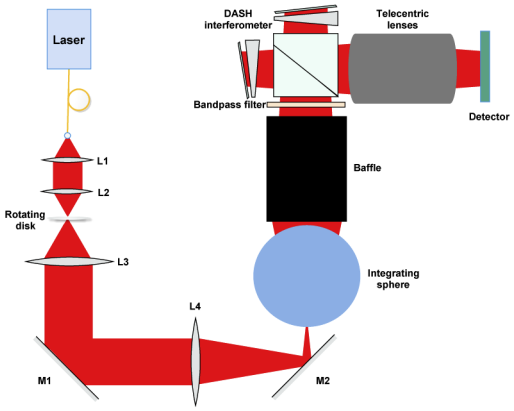

Fig. 6. Schematic of the laboratory test setup. The different monochromatic homogeneous illumination is obtained by the combination of tunable laser and integrating sphere. L denotes lenses, and M denotes mirrors.

spatial frequency destroys the binning process calculating the average value of several rows of inteferograms. Fortunately, the effect of the Y-direction component of spatial frequency and other optical defects can be corrected [27] and the corrected fringe image is shown in Fig. 7(b). Except for the remaining distortions on the edges, the tilts and distortions of the stripes have been corrected.

The interference visibility can be estimated by the ratio of the signal amplitude to the signal direct current (DC) bias. The signal-modulated portion can be isolated using a suitable isolation window and backward transformation in the spectrum domain [12]. Then the signal amplitude can be calculated from the modulus of the isolated signal. Implementing the inverse Fourier transform for the isolated DC component in the spectrum domain also yields the signal DC bias. Accordingly, an interferogram at the center of Fig. 7(a) is shown in Fig. 8(a) and its visibility as a function of position is estimated in Fig. 8(b). The estimated envelope is the sum of signal amplitude and signal DC bias. The good evaluation of the interferogram envelope in Fig. 8(a) verifies the accurate determinations of the signal amplitude and the signal DC bias. Fig. 8(b) indicates that all of the visibilities are larger than 0.8 in general and the maximum value achieves 0.94 when 9° field-of-view illumination is applied. The serious declines appear on the both sides of the envelope and the visibility, which is related to the endpoint-discontinuity artifacts. The estimations of envelope and visibility are not correct in this region.

Optics EXPRESS

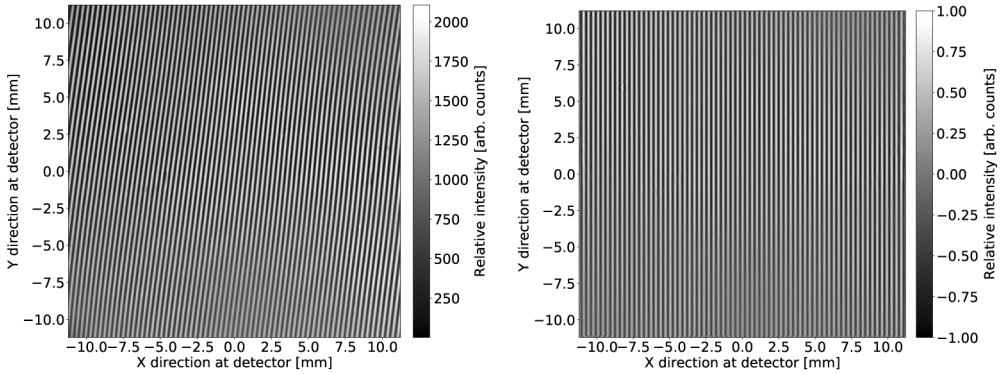

(a) (b)

Fig. 7. Measured fringe image at a wavelength of 630.03 nm when the 4.5-degree half cone angle radiation illuminates the interferometer (a) and the corrected fringe image after flat-field correction [28] and phase distortion correction [27] (b). A 2048×2048 detector with 11 um pixel size is applied to record the fringes and the exposure time is several seconds. Only a modulated portion is reserved after the corrections, hence the relative intensity change in (b) comparing with (a).

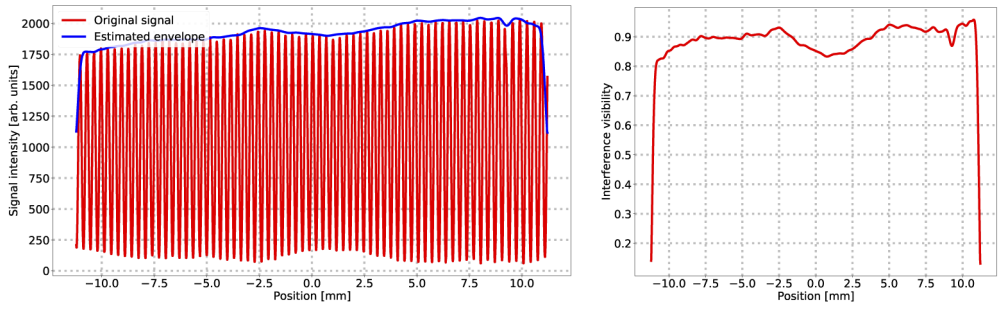

(a) (b)

Fig. 8. Left panel (a), the slice interferogram at the center of the fringe image in Fig. 7(a) and the corresponding envelope. Right panel (b), the visibility distribution of the slice interferogram plotted in the left panel.

Optics EXPRESS

The Littrow angle determining the interferogram spatial frequency can be characterized based on the setup of Fig. 6 using a tunable laser. Two methods, phase analysis and spectrum analysis, are discussed to determine the spatial frequency. The phase of an interferogram can be determined by calculating the arctangent value of the ratio of the imaginary part and real part of the modulated component [12]. Then the spatial frequency can be considered as the quotient of the rate of phase change with position and 2π. For the spectrum analysis, the corresponding spatial frequency of the spectrum peak corresponds to the interferogram spatial frequency. In order to compare the Littrow angles and Littrow wavelengths of different regions, the detector was divided into 3 sub-regions from the bottom to the top. For each sub-region or whole detector, a two-dimensional Fourier transform was applied to the fringe image to produce a two-dimensional spectrum, which was then averaged to obtain a one-dimensional spectrum. Note that both the phase analysis and the spectrum analysis are based on the one-dimensional spectrum obtained. Fitting a linear function to the measured points yields the relation between the spatial frequency and the input wavenumber shown in Fig. 9. The results calculated from two methods are in good agreement with 99.999% consistency. The retrieved Littrow angles using the averages of the whole detector, rows 45-694, rows 695-1344 and rows 1345-1994 are 16.49363°, 16.49362°, 16.49380° and 16.49460°, respectively. Obviously, the vertical variation exists especially in the top region, and the Littrow angle becomes larger in the region closer to the top, which may be caused by the asymmetry of the beamsplitter, field-widening prism and diffraction grating.

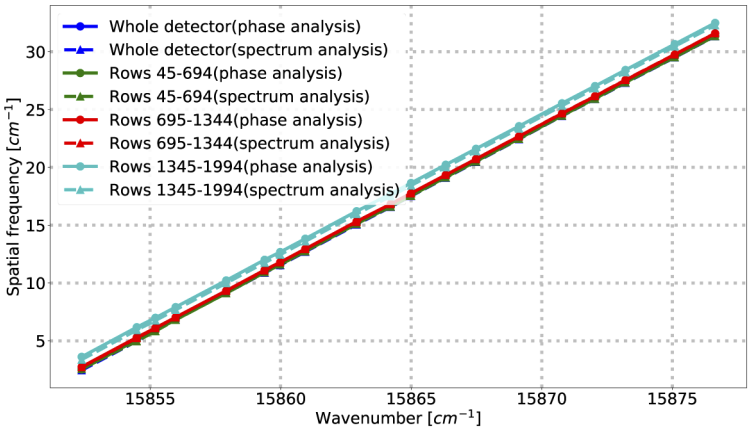

Fig. 9. Interferogram spatial frequency function of the emission wavenumber. All of the wavelengths and wavenumbers are given with respect to air. During the spectrum analysis, zero padding by a factor of 100 is added for each row of the interferogram before the Fourier transform.

5. Thermal performance

A similar system in Fig. 6 was built for the thermal performance test. Instead of laser light, a frequency-stable neon lamp was utilized here. The interferometer was contained in an aluminium housing where the temperature was stabilized under a PID (proportional-integral-derivative) controller with an accuracy of 0.1 °C. The ambient temperature was also controlled using the air condition with a temperature of 20 °C. The measurements were performed from 22 °C to 30 °C with an interval of 1 °C. When a thermal equilibrium was established in the housing, 10 frames of the interferograms for each temperature were recorded with an exposure time of 30 seconds. Then the mean value of the 10 frames, equivalent to the typical exposure time in ground-based nightglow observation, was calculated for further analysis. For each interferogram, the flat-field correction and the phase-distortion correction using identical phase-distortion parameters was

Optics EXPRESS

implemented. The 500-row signal near the center of the fringe image was then averaged to derive the phase change. The phase change can be directly retrieved based on the Hilbert transform described in [19] or according to the following equation,

$$\Delta\varphi(x) = \varphi_2(x) - \varphi_1(x) = \arctan\left\{\frac{\Im[I_2(x)]\,\Re[I_1(x)] - \Re[I_2(x)]\,\Im[I_1(x)]}{\Re[I_2(x)]\,\Re[I_1(x)] + \Im[I_2(x)]\,\Im[I_1(x)]}\right\}, \tag{9}$$

where $\Im\left[I_{1,2}(x)\right]$ and $\Re\left[I_{1,2}(x)\right]$ represent the imaginary and real parts of the signal-modulated portion, respectively. A linear function $\Delta\varphi(x)$ was fitted to the retrieved phase change distribution and the fitting result shows the change of spatial frequency (slope divided by 2π) and phase offset (intercept) due to the temperature variation.

As discussed in [29], a predictive model using ray-trace software and a finite element analysis can be built. The model can adjust the parameters including the refractive index, the grating groove density and the dimensions of the elements according to the respective ambient temperature. Note that all of the dimensions and angles are provided with the manufacturer's inspection data and the material data are based on the glass catalogs [30,31]. The mechanical deformations resulting from the differential expansion between two different materials were characterized by a finite element model (FEM) analysis. A linear static stress model considering the monolithic interferometer, the covers and the 5-mm adhesive layers between the interferometer and the covers was established and the deformation (relative position change) result is shown in Fig. 10. After adding the deformation into every element, the new angles were calculated by fitting the updated plane. On arm one, the distortions on the angle between field-widening prism and beamsplitter and the angle between field-widening prism and grating are -1.466×10^{-6} radians/°C and 4.111×10^{-7} radians/°C, respectively. The corresponding distortions on arm two are -1.119×10^{-6} radians/°C and 7.623×10^{-7} radians/°C. Updating the angles in the ray-trace model, the Littrow angle and the optical OPD offset at different temperatures were tracked. The spatial frequency and the phase offset were therefore also monitored in this predictive model.

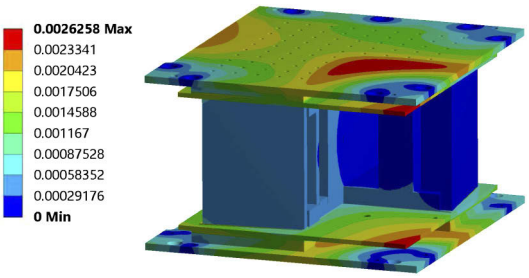

Fig. 10. Deformation of the interferometer based on a finite element model. The analysis includes 3059857 nodes and 1400125 elements with the fixed constraints on the screw holes. Note that the top and bottom plates are the covers of the interferometer housing and the unit of the legend is millimeter.

Figure 11(a) and Fig. 11(b) show how the spatial frequency and the phase offset change in the measurements and the model study when the temperature changes. As the temperature increases, the spatial frequencies increase linearly at 0.0154 cm^{-1}/°C in the measurements and 0.0313 cm^{-1}/°C in the model study, respectively. Similarly, the phase offsets change at linear rates of 0.469 rad/°C in the measurements and 0.330 rad/°C in the model study, respectively. The thermal drift of the spatial frequency agrees with the model value within a factor of two, and the thermal drift of the phase offset agrees with the model value within 29.6%. It was possible to vary the air pressure during the measurement, but we did not consider this effect in the model study. In addition, the parameters of uncertainty and alignment tolerances cause the measurements and the model to differ further.

Optics EXPRESS

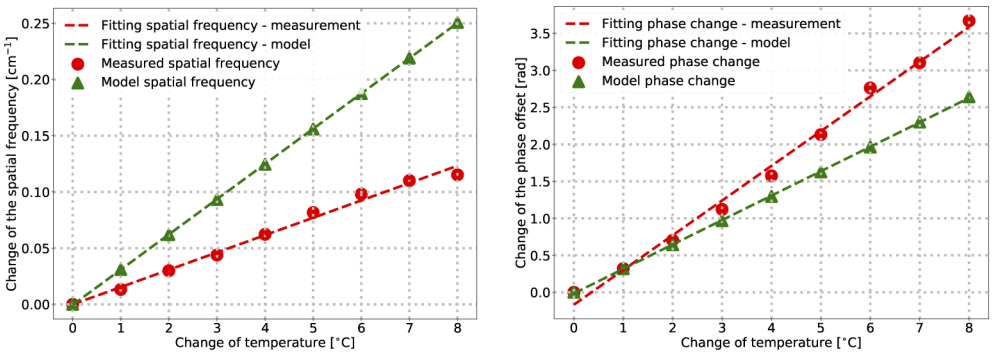

(a) (b)

Fig. 11. Change of the spatial frequency (a) and change of the phase offset (b) when the temperature is varied from 22 °C to 30 °C. Note that the dashed lines are the fitting results, the red lines are the measurement results and the green lines are the model results.

Compared with other DASH interferometers with a phase drift of 1.25 rad/°C [13] and 4.29 rad/°C [29], a more stable DASH interferometer has been realized. However, the temperature response (0.469 rad/°C) is still higher than the design value (1.2 mrad/°C) due to the manufacturing and alignment tolerances. Temperature control and calibration thermal tracking are also necessary during wind measurement for this interferometer. UV curing adhesive was used to glue the separate optical components, and the thermal coefficient of adhesive is an order of magnitude larger than the thermal expansion coefficient of H-FK61 [32]. In order to compensate the incoincidence of the two grating images caused by manufacturing and alignment tolerances, the difference of adhesive thickness between two arms is inevitable during final gluing. Therefore, the variation of adhesive thickness on two arms seriously deteriorates the expected thermal compensation. In order to achieve better thermal stability, a more thermally stable adhesive and a more precise alignment are suggested during the interferometer assembly.

6. Summary

We studied a monolithic DASH interferometer with field-widening and thermal compensation from the aspects of optical design and laboratory performance. An optimum OPD offset was chosen to mitigate the contradiction between increasing phase sensitivity and visibility decline. The thermal drift of a monolithic DASH interferometer can be compensated by a suitable combination of different glasses and dimensions, which was verified in the laboratory test. A thermally stable monolithic DASH interferometer with large etendue was designed and built. The field of view test showed that the high contrast of the fringes is maintained when the field of view reaches 9°. The temperature dependence of the phase offset and the spatial frequency were determined with thermal sensitivities of 0.469 rad/°C and 0.0154 cm^{-1}/°C, respectively. Nevertheless, a better thermal stability of DASH interferometer can be realized with higher manufacturing tolerance and more precise assembly.

The design and laboratory performance indicate that this DASH instrument meets the requirement to observe the thermospheric wind from the ground. A compact and rugged DASH instrument suited for the field measurement will be developed in the next step, and the field measurements will be carried out with this DASH sensor in the future.

Optics EXPRESS

Funding

China Scholarship Council; Forschungszentrum Jülich; Bergische Universität Wuppertal; National Space Science Center, Chinese Academy of Science(NSSC, CAS).

Acknowledgements

The authors would like to thank Qiuyu Chen, Oliver Wroblowski and Heinz Rongen for their assistance and valuable discussion.

Disclosures

The authors declare no conflicts of interest.

References

1. J. K. Hargreaves, *The solar-terrestrial environment: an introduction to geospace-the science of the terrestrial upper atmosphere, ionosphere, and magnetosphere* (Cambridge University, 1992).
2. M. H. Rees and N. Rees, *Physics and chemistry of the upper atmosphere*, vol. 1 (Cambridge University, 1989).
3. J. J. Makela, J. W. Meriwether, J. P. Lima, E. S. Miller, and S. J. Armstrong, "The remote equatorial nighttime observatory of ionospheric regions project and the international heliospherical year," Earth, Moon, Planets **104**(1-4), 211–226 (2009).
4. P. Sultan, "Linear theory and modeling of the rayleigh-taylor instability leading to the occurrence of equatorial spread f," J. Geophys. Res.: Space Phys. **101**(A12), 26875–26891 (1996).
5. P. B. Hays, V. J. Abreu, M. E. Dobbs, D. A. Gell, H. J. Grassl, and W. R. Skinner, "The high-resolution doppler imager on the upper atmosphere research satellite," J. Geophys. Res.: Atmos. **98**(D6), 10713–10723 (1993).
6. T. Killeen, Q. Wu, S. Solomon, D. Ortland, W. Skinner, R. Niciejewski, and D. Gell, "TIMED doppler interferometer: Overview and recent results," J. Geophys. Res.: Space Phys. **111**(A10), A10S01 (2006).
7. G. G. Shepherd, W. A. Gault, D. Miller, Z. Pasturczyk, S. F. Johnston, P. Kosteniuk, J. Haslett, D. J. Kendall, and J. Wimperis, "WAMDII: wide-angle michelson doppler imaging interferometer for spacelab," Appl. Opt. **24**(11), 1571–1584 (1985).
8. G. G. Shepherd, G. Thuillier, W. Gault, B. Solheim, C. Hersom, J. Alunni, J.-F. Brun, S. Brune, P. Charlot, L. Cogger, D. Desaulniers, W. Evans, R. Gattinger, F. Girod, D. Harvier, R. Hum, D. Kendall, E. Llewellyn, R. Lowe, J. Ohrt, F. Pasternak, O. Peillet, I. Powell, Y. Rochon, W. Ward, R. Wiens, J. Wimperis, and L. Cogger, "WINDII, the wind imaging interferometer on the upper atmosphere research satellite," J. Geophys. Res.: Atmos. **98**(D6), 10725–10750 (1993).
9. J. Meriwether, "Studies of thermospheric dynamics with a fabry–perot interferometer network: A review," J. Atmos. Sol.-Terr. Phys. **68**(13), 1576–1589 (2006).
10. J. M. Harlander, F. L. Roesler, J. G. Cardon, C. R. Englert, and R. R. Conway, "Shimmer: a spatial heterodyne spectrometer for remote sensing of earth' middle atmosphere," Appl. Opt. **41**(7), 1343–1352 (2002).
11. M. Kaufmann, F. Olschewski, K. Mantel, B. Solheim, G. Shepherd, M. Deiml, J. Liu, R. Song, Q. Chen, O. Wroblowski, D. Wei, Y. Zhu, F. Wagner, F. Loosen, D. Froehlich, T. Neubert, H. Rongen, P. Knieling, P. Toumpas, J. Shan, G. Tang, R. Koppmann, and M. Riese, "A highly miniaturized satellite payload based on a spatial heterodyne spectrometer for atmospheric temperature measurements in the mesosphere and lower thermosphere," Atmos. Meas. Tech. **11**(7), 3861–3870 (2018).
12. C. R. Englert, D. D. Babcock, and J. M. Harlander, "Doppler asymmetric spatial heterodyne spectroscopy (DASH): concept and experimental demonstration," Appl. Opt. **46**(29), 7297–7307 (2007).
13. J. M. Harlander, C. R. Englert, D. D. Babcock, and F. L. Roesler, "Design and laboratory tests of a doppler asymmetric spatial heterodyne (DASH) interferometer for upper atmospheric wind and temperature observations," Opt. Express **18**(25), 26430–26440 (2010).
14. C. R. Englert, J. M. Harlander, J. T. Emmert, D. D. Babcock, and F. L. Roesler, "Initial ground-based thermospheric wind measurements using doppler asymmetric spatial heterodyne spectroscopy (DASH)," Opt. Express **18**(26), 27416–27430 (2010).
15. J. M. Harlander, C. R. Englert, C. M. Brown, K. D. Marr, I. J. Miller, V. Zastera, B. W. Bach, and S. B. Mende, "Michelson interferometer for global high-resolution thermospheric imaging (MIGHTI): monolithic interferometer design and test," Space Sci. Rev. **212**(1-2), 601–613 (2017).
16. C. R. Englert, J. M. Harlander, C. M. Brown, K. D. Marr, I. J. Miller, J. E. Stump, J. Hancock, J. Q. Peterson, J. Kumler, W. H. Morrow, T. Mooney, S. Ellis, S. Mende, S. Harris, M. Stevens, J. Makela, B. Harding, and T. Immel, "Michelson interferometer for global high-resolution thermospheric imaging (MIGHTI): instrument design and calibration," Space Sci. Rev. **212**(1-2), 553–584 (2017).
17. G. Jiang, J. Xu, W. Yuan, B. Ning, W. Wan, and L. Hu, "A comparison of mesospheric winds measured by FPI and meteor radar located at 40n," Sci. China: Technol. Sci. **55**(5), 1245–1250 (2012).

Optics EXPRESS

18. J. Emmert, M. Faivre, G. Hernandez, M. Jarvis, J. Meriwether, R. Niciejewski, D. Sipler, and C. Tepley, "Climatologies of nighttime upper thermospheric winds measured by ground-based fabry-perot interferometers during geomagnetically quiet conditions: 1. local time, latitudinal, seasonal, and solar cycle dependence," J. Geophys. Res.: Space Phys. **111**(A12), A12303 (2006).
19. J. Liu, D. Wei, Y. Zhu, M. Kaufmann, F. Olschewski, K. Mantel, J. Xu, and M. Riese, "Effective wind and temperature retrieval from doppler asymmetric spatial heterodyne spectrometer interferograms," Appl. Opt. **57**(30), 8829–8835 (2018).
20. C. Englert, J. Harlander, C. Brown, J. Meriwether, J. J. Makela, M. Castelaz, J. Emmert, D. Drob, and K. Marr, "Coincident thermospheric wind measurements using ground-based doppler asymmetric spatial heterodyne (DASH) and fabry–perot interferometer (FPI) instruments," J. Atmos. Sol.-Terr. Phys. **86**, 92–98 (2012).
21. L. Cogger, J. Walker, J. Meriwether Jr, and R. Burnside, "F region airglow: Are ground-based observations consistent with recent satellite results?" J. Geophys. Res.: Space Phys. **85**(A6), 3013–3020 (1980).
22. R. Link and L. Cogger, "A reexamination of the oi 6300-å nightglow," J. Geophys. Res.: Space Phys. **93**(A9), 9883–9892 (1988).
23. G. Thuillier and G. G. Shepherd, "Fully compensated michelson interferometer of fixed-path difference," Appl. Opt. **24**(11), 1599–1603 (1985).
24. G. Thuillier and M. Hersé, "Thermally stable field compensated michelson interferometer for measurement of temperature and wind of the planetary atmospheres," Appl. Opt. **30**(10), 1210–1220 (1991).
25. J. Harlander, R. J. Reynolds, and F. L. Roesler, "Spatial heterodyne spectroscopy for the exploration of diffuse interstellar emission lines at far-ultraviolet wavelengths," Astrophys. J. **396**, 730–740 (1992).
26. J. M. Harlander, "Spatial heterodyne spectroscopy: Interferometric performance at any wavelength without scanning," Ph.D. thesis (1991).
27. C. R. Englert, J. M. Harlander, J. G. Cardon, and F. L. Roesler, "Correction of phase distortion in spatial heterodyne spectroscopy," Appl. Opt. **43**(36), 6680–6687 (2004).
28. C. R. Englert and J. M. Harlander, "Flatfielding in spatial heterodyne spectroscopy," Appl. Opt. **45**(19), 4583–4590 (2006).
29. K. D. Marr, C. R. Englert, J. M. Harlander, and K. W. Miller, "Thermal sensitivity of dash interferometers: the role of thermal effects during the calibration of an echelle DASH interferometer," Appl. Opt. **52**(33), 8082–8088 (2013).
30. SCHOTT Advance Optics, "Optical Glass - Overview," https://www.schott.com/advanced_optics/english/download/index.html (2019).
31. CDGM GLASS CO.,LTD, "OPTICAL GLASS DATABASE," http://www.cdgmgd.com/database/toWebDatabase.htm?k=Products_Data&url=database (2018).
32. Norland Products, "Norland Optical Adhesive 61," https://www.norlandprod.com/adhesives/NOA%2061.html (2020).